JOURNAL OF COMPUTATIONAL PHYSICS 66, 481–507 (1986)

Dynamic Modeling of Transport and Positional Control of Tokamaks

S. C. JARDIN, N. POMPHREY, AND J. DELUCIA

Plasma Physics Laboratory, Princeton University, Princeton, New Jersey 08544

Received August 29, 1985; revised December 5, 1985

DEDICATED TO THE MEMORY OF RAYMOND C. GRIMM

We describe a numerical model of a free boundary axisymmetric tokamak plasma and its associated control systems. The plasma is modeled with a hybrid method using two-dimensional velocity and flux functions with surface-averaged MHD equations describing the evolution of the adiabatic invariants. Equations are solved for the external circuits and for the effects of eddy currents in nearby conductors. The method is verified by application to several test problems and used to simulate the formation of a bean-shaped plasma in the PBX experiment.

I. INTRODUCTION

There is a growing body of evidence from both theoretical and experimental studies that tokamaks with shaped, noncircular cross-sections offer significant advantages over conventional circular cross-section tokamaks [1]. Onset conditions for ideal magnetohydrodynamic (MHD) instabilities, resistive tearing instabilities, beam-driven plasma instabilities, and the amplitude of residual microinstabilities are all expected to improve when the tokamak cross section becomes noncircular [2–5]. The ohmic heating power is also increased and transport is expected to improve.

However, there are several disadvantages associated with these tokamaks. The external shaping fields must be carefully programmed to establish the desired configuration. Also the positional control problems are compounded. In the absence of nearby conducting walls, the plasma is generally unstable to an axisymmetric displacement. Close fitting passive conductors can normally slow down these instabilities to times comparable to the resistive time of the conductors, but active feedback systems are generally necessary to provide complete stability [6, 7]. The time scales over which the external shaping fields change and the feedback systems respond are generally comparable to the resistive diffusion time of the plasma.

This paper describes a computational mathematical model developed to study the control requirements for shaping tokamak discharges. The model consists of a two-dimensional transport description of a plasma interacting with a discrete set of

0021-9991/86 $3.00

axisymmetric conductors which obey circuit equations with active feedback amplifiers being included. A solution method is utilized in which the plasma force balance equation is modified by scaling up the plasma mass and viscosity. This technique keeps the plasma in near force balance equilibrium while alleviating the severe time scale discrepancy between wave-like and diffusion-like phenomena. Also the vacuum equations are modified to describe a very high resistivity zero pressure plasma. The parameter scaling does not affect the bulk motion of a tokamak plasma that is stable on the ideal MHD time scale.

In the following sections we present the modified equations, discuss the relevant time scales, and present the numerical methods utilized in the simulation. We verify the computational technique in Section V by computing several test problems in some detail. Then in Section VI we apply this method to the modeling of an actual tokamak experiment, the Princeton Beta Experiment (PBX) [8]. It is shown that a system of shaping coils plus passive and active feedback conductors should be sufficient to shape the tokamak into a kidney bean shape and hold it there in a controlled manner.

II. Equations

In an axisymmetric toroidal geometry with symmetry angle ϕ, the magnetic field is expressible in terms of the poloidal flux per radian Ψ and the toroidal field function g in the standard way

$$\mathbf{B} = \nabla\phi \times \nabla\Psi + g\nabla\phi. \tag{1}$$

The function g is a general two-dimensional function whose contours will align themselves with constant poloidal flux contours when the system is in static force balance, i.e., $g = g(\Psi)$ in equilibrium. The toroidal flux Φ within a constant Ψ contour $\Psi = \Psi_c$ is obtained by performing an integral over the contour's interior

$$\Phi \equiv \frac{1}{2\pi}\int_{\Psi<\Psi_c} d\tau\, \mathbf{B}\cdot\nabla\phi = \int_{\Psi<\Psi_c} dx dz\, \frac{g(x,z)}{x}, \tag{2}$$

where (x, ϕ, z) form a cylindrical coordinate system (Fig. 1).

We find it advantageous to express the plasma momentum density $\mathbf{m} = M_i n \mathbf{v}$ in terms of a stream function A, a toroidal component ω, and a potential Ω, thus

$$\mathbf{m} = \nabla\phi \times \nabla A + \omega\nabla\phi + \nabla\Omega. \tag{3}$$

This form for the velocity field allows separate numerical treatment of the incompressible and compressible parts of the flow field. Since the physics governing the wave dynamics of $\nabla\cdot\mathbf{m} = \nabla^2\Omega$ and $\nabla\phi\cdot\nabla\times\mathbf{m} = \nabla\cdot x^{-2}\nabla A$ are determined, respectively, by the longitudinal and transverse characteristics, the time evolution of these

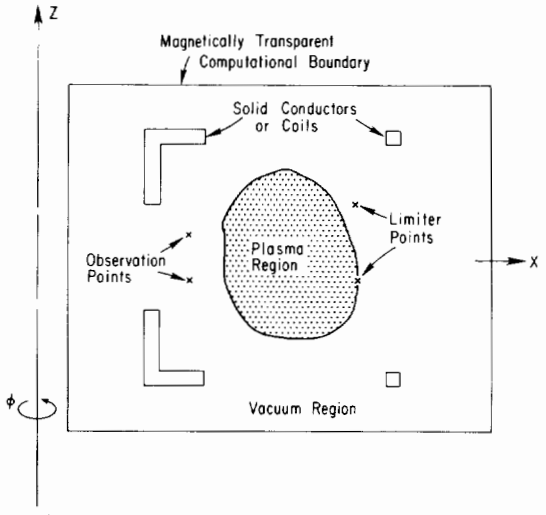

FIG. 1. Computational Domain: Inside a magnetically transparent boundary are a plasma region, a vacuum region, and one or more solid conductor regions. The plasma vacuum interface is in contact with a limiter point. Observation points measure the poloidal flux versus time.

two quantities can be quite different. The numerical method presented in Section III makes use of this representation to deal with the time scale disparity.

We describe here the set of dynamical equations solved in the computational domain illustrated in Fig. 1. We take a uniform Cartesian spatial mesh and divide it into three regions: the plasma region, the vacuum region, and the solid conductors. The interface between the plasma and the vacuum regions will change in time, being defined as the first poloidal flux surface $\Psi = \text{const.}$ touching a limiter point or containing an x-point (magnetic limiter). The description is "free boundary" in that the computational boundary is not a physical boundary. The magnetic field is updated on it so that its placement will not affect the plasma evolution.

In each region, a modified form of the MHD-Maxwell equations are solved. The modifications take the form of introducing several continuous parameters such that the true (inertialess) MHD and vacuum equations are obtained when these parameters approach zero. These parameters are the enhanced plasma mass density and viscosity, and the electrical conductivity of the vacuum region. For finite values of these parameters, the equations do not change their type across region boundaries, and solutions remain continuous. We describe next the exact equations solved in each region.

A. *Plasma Region*

We are concerned with obtaining accurate solutions to the resistive MHD equations on the time scale governed by resistive dissipation and cross field transport in the plasma, and by the rate of change of the currents in the poloidal field circuits due to resistivity and to externally applied driving voltages. This time scale

is long compared to the time it takes for densities and temperatures to equilibrate along the magnetic field lines so that we can take these quantities to be one-dimensional spatial functions, uniform on each magnetic surface. It is also long compared to the time that Alfvén waves act to equilibrate force imbalances so that the static equilibrium condition $\mathbf{J} \times \mathbf{B} = \nabla p$ will remain nearly satisfied.

In the absence of Alfvén transit time scale (ideal MHD) instabilities, the inertial terms in the plasma force balance equation are negligible. They are smaller than the magnetic forces by the square of the inverse magnetic Reynolds number, S_M^{-2}, where

$$S_M^{-1} = \left(\frac{\eta}{aB_0}\right)\left(\frac{nM_i}{\mu_0}\right)^{1/2} \ll 1. \tag{4}$$

with η the plasma resistivity and a the minor radius. Since the magnitude of the true time-averaged inertial terms are small, we replace them with a more convenient *modified* inertial term which is equivalent to enhancing the plasma mass, dropping the convective derivative term, and choosing a specific form for the plasma viscosity operator,

$$\mathbf{F}_v(\mathbf{m}) = -\nu_1[\nabla^2\mathbf{m} - \nabla(\nabla \cdot \mathbf{m})] - \nu_2\nabla(\nabla \cdot \mathbf{m}). \tag{5}$$

Thus the plasma force balance equation becomes

$$\frac{\partial \mathbf{m}}{\partial t} + \mathbf{F}_v(\mathbf{m}) = \mathbf{J} \times \mathbf{B} - \nabla p. \tag{6}$$

The mass enhancement and viscosity parameters are chosen so that the left-hand side of Eq. (6) remains small enough to be negligible compared to the right-hand side, but not so small as to make forward time integration prohibitive. Further motivation for the modified inertial technique is given in Ref. [9]. It must be verified a posteriori that the modified inertial terms indeed remain small and that the physical results are independent of the fictitious mass and viscosity values over a wide range.

Scalar forms of the momentum equations are obtained by operating on the modified force balance equation, Eq. (6) with $\{\nabla\cdot\}$, $\{\nabla\phi \cdot \nabla\times\}$, and $\{\nabla\phi\cdot\}$. Thus, we obtain

$$\frac{\partial}{\partial t}\nabla^2\Omega + \nabla\cdot\left[\frac{\Delta^*\Psi}{\mu_0 x^2}\nabla\Psi + \frac{g}{\mu_0 x^2}\nabla g + \nabla p - \nu_2\nabla(\nabla^2\Omega)\right] = 0, \tag{6a}$$

$$\frac{\partial}{\partial t}\Delta^* A + x^2\nabla\cdot\left[\frac{\Delta^*\Psi}{\mu_0 x^2}\nabla\Psi\times\nabla\phi + \frac{g}{\mu_0 x^2}\nabla g\times\nabla\phi - \frac{\nu_1}{x^2}\nabla(\Delta^* A)\right] = 0, \tag{6b}$$

$$\frac{\partial}{\partial t}\omega + \mu_0^{-1}\nabla\phi\times\nabla g\cdot\nabla\Psi - \nu_1\Delta^*\omega = 0, \tag{6c}$$

where $\Delta^* \equiv x^2\nabla\cdot x^{-2}\nabla$ is the standard toroidal elliptic operator.

We note here that static solutions to Eqs. (6a)–(6c) with (Ω, A, ω) and their time derivatives set to zero are exact solutions to the full Grad–Shafranov equilibrium equation, i.e.,

$$\Delta^*\Psi + \mu_0 x^2 \frac{d}{d\Psi} p(\Psi) + \frac{1}{2}\frac{d}{d\Psi} g^2(\Psi) = 0. \tag{7}$$

Transient solutions for Ψ, p, and g are always within $\varepsilon \equiv S_M^{-2}$ of satisfying Eq. (7).

Faraday's Law, and an Ohm's law of the form

$$\mathbf{E} + \mathbf{v} \times \mathbf{B} = \mathbf{R}, \tag{8}$$

where $\mathbf{R}$ contains the nonideal terms, yield evolution equations for the poloidal flux and toroidal field functions

$$\frac{\partial}{\partial t}\Psi + \frac{1}{\rho_0}(\nabla\phi \times \nabla A \cdot \nabla\Psi + \nabla\Omega \cdot \nabla\Psi) = x^2 \nabla\phi \cdot \mathbf{R}, \tag{9}$$

$$\frac{\partial}{\partial t} g + x^2 \nabla \cdot \left[\frac{g}{\rho_0 x^2}(\nabla\phi \times \nabla A + \nabla\Omega) - \frac{\omega}{\rho_0 x^2}\nabla\phi \times \nabla\Psi - \nabla\phi \times \mathbf{R} \right] = 0. \tag{10}$$

Here, $\rho_0 \equiv n_0 M_i$ is a constant, having the role of the enhanced mass density.

Since the toroidal magnetic field is due primarily to external currents, it is relatively immobile, making it convenient to evolve the surface-averaged thermodynamic variables relative to magnetic coordinate surfaces containing a fixed amount of toroidal flux. To derive the surface-averaged evolution equations, we decompose the cross-field fluid velocity into two parts

$$\mathbf{v} \cdot \nabla\Psi = \mathbf{v}_c \cdot \nabla\Psi + \mathbf{v}_R \cdot \nabla\Psi, \tag{11}$$

where $\mathbf{v}_c \cdot \nabla\Psi$ is associated with the evolution of the coordinate surfaces, and $\mathbf{v}_R \cdot \nabla\Psi$ is the fluid flow relative to these surfaces. For magnetic coordinate surfaces evolving with fixed toroidal flux Φ, we have from Eq. (10),

$$\mathbf{v}_R \cdot \nabla\Psi = \frac{x^2}{g}\nabla\phi \times \mathbf{R} \cdot \nabla\Psi \tag{12}$$

and

$$\frac{\partial}{\partial t}\left(\frac{1}{q}\oint \frac{dl}{B_p}\right) = \frac{\partial}{\partial\Psi}\left(\frac{1}{q}\oint \frac{dl}{B_p}\mathbf{v}_c \cdot \nabla\Psi\right). \tag{13}$$

Here, $q \equiv (2\pi)^{-1}\,\partial\Phi/\partial\Psi$ is the safety factor, $B_p \equiv |\nabla\phi \times \nabla\Psi|$ is the magnitude of the poloidal magnetic field, and the line integrals are around a contour in a poloidal cross section at $\Psi = \text{const}$. Using Eqs. (11)–(13) to eliminate the velocity from the mass and energy conservation equations, we obtain [10] one-dimensional evolution equations for the differential number density $N' \equiv n\,\partial V/\partial\Phi$, and the dif-

ferential total and electron entropy densitities $\sigma \equiv p(\partial V/\partial \Phi)^{5/3}$ and $\sigma_e \equiv p_e(\partial V/\partial \Phi)^{5/3}$, with respect to magnetic surfaces containing a fixed toroidal flux.

$$\frac{\partial}{\partial t} N' = -\frac{\partial}{\partial \Phi}(N'\Gamma) + S_N, \tag{14}$$

$$\frac{\partial}{\partial t}\sigma = \frac{2}{3}\left(\frac{\partial V}{\partial \Phi}\right)^{2/3}\left[V_L \frac{\partial K}{\partial \Phi} - \frac{\partial}{\partial \Phi}(Q_i + Q_e) + \frac{\partial V}{\partial \Phi}(S_e + S_i)\right], \tag{15}$$

$$\frac{\partial}{\partial t}\sigma_e = \frac{2}{3}\left(\frac{\partial V}{\partial \Phi}\right)^{2/3}\left[V_L \frac{\partial K}{\partial \Phi} - \frac{\partial Q_e}{\partial \Phi} + \frac{\partial V}{\partial \Phi}\left(-\Gamma \frac{\partial p_i}{\partial \Phi} + Q_{\Delta e} + S_e\right)\right]. \tag{16}$$

Time derivatives are with respect to surfaces containing fixed toroidal flux Φ. We have defined the differential volume

$$\frac{\partial V}{\partial \Phi} = \frac{\partial}{\partial \Phi}\oint d\tau = \frac{1}{q}\oint \frac{dl}{B_p}, \tag{17}$$

the loop voltage

$$V_L = \frac{2\pi \langle \mathbf{R}\cdot\mathbf{B}\rangle}{\langle \mathbf{B}\cdot\nabla\phi\rangle}, \tag{18}$$

and the total toroidal current within a flux surface

$$K = \oint \mathbf{B}_p \cdot \mathbf{dl} = \oint \frac{dl|\nabla\Psi|}{x}. \tag{19}$$

The particle flux and electron and ion heat fluxes are defined as

$$\Gamma = 2\pi q[\langle x^2 \mathbf{R}\cdot\nabla\phi\rangle - \langle \mathbf{R}\cdot\mathbf{B}\rangle/\langle B\cdot\nabla\phi\rangle], \tag{20}$$

$$Q_i = \frac{\partial V}{\partial \Phi}\left[\langle \mathbf{q}_i\cdot\nabla\Phi\rangle + \frac{5}{2}p_i\Gamma\right], \tag{21}$$

$$Q_e = \frac{\partial V}{\partial \Phi}\left[\langle \mathbf{q}_e\cdot\nabla\Phi\rangle + \frac{5}{2}p_e\Gamma\right], \tag{22}$$

where $\mathbf{q}_i$ and $\mathbf{q}_e$ are the random heat flux vectors. We have introduced the flux surface average operator in Eqs. (18), (20), (21), (22),

$$\langle a\rangle \equiv \frac{\oint (dl/B_p)\, a}{\oint (dl/B_p)}.$$

The equipartition term is classical

$$Q_{\Delta e} = 3\left(\frac{\omega_{pi}^2}{\mu_0 c^2}\right)\eta_\perp n_e (T_i - T_e) \tag{23}$$

with $\eta_\perp = 2.0\,\eta_\parallel$ the perpendicular resistivity. The S_n, S_e, S_i are external sources of particles, electron energy, and ion energy.

We note here that Eqs. (9) and (10) imply an evolution equation for the transform $\iota \equiv q^{-1}$,

$$\frac{\partial}{\partial t}\iota = \frac{\partial}{\partial \Phi} V_L. \tag{24}$$

Equation (24) is redundant, but can serve as a check and possibly also as a corrector to the Ψ and g functions evolved through Eqs. (9) and (10). The correction feature is discussed in Section IIIB.

We take the nonideal dissipation vector $\mathbf{R}$ in Eq. (8) to consist of a classical part $\mathbf{R}_c$ and an anomalous part $\mathbf{R}_A$, perpendicular to the magnetic field

$$\mathbf{R} = \mathbf{R}_c + B^{-2}\mathbf{B} \times \mathbf{R}_A \times \mathbf{B}. \tag{25}$$

For the classical part we take

$$\mathbf{R}_c = \eta_\parallel \mathbf{J} \tag{26}$$

with $\eta_\parallel = 0.51 \times 10^{-4} Z \ln \Lambda T_e^{-3/2}$ ohms when the electron temperature T_e is measured in electron volts. Here, $T_e = k_B^{-1} p_e/n$ as determined from Eqs. (14) and (16). In evolving the 2-D flux functions Ψ and g in Eqs. (9) and (10), it is permissible to take $\mathbf{R} = \mathbf{R}_c$, since the anomalous $\mathbf{R}_A$ is perpendicular to $\mathbf{B}$. Including $\mathbf{R}_A$ in Eqs. (9) and (10) would be equivalent to using a slightly modified velocity field $\mathbf{v}' = \mathbf{v} + \mathbf{R}_A \times \mathbf{B}/B^2$ which would lead to no additional flux diffusion. Thus, in Eqs. (9) and (10), we can evaluate

$$x^2 \nabla\phi \cdot \mathbf{R}_c = \frac{\eta_\parallel}{\mu_0} \Delta^* \Psi, \tag{27}$$

$$\nabla\phi \times \mathbf{R}_c = \frac{\eta_\parallel}{\mu_0 x^2} \nabla g, \tag{28}$$

while in Eq. (18), an explicit expression for the loop voltage can be obtained

$$V_L = \eta_\parallel \frac{(2\pi q)^2}{\alpha^2} \frac{\partial}{\partial \Phi} (\alpha K \iota), \tag{29}$$

where we have defined

$$\alpha \equiv \frac{2\pi q}{g} = \oint \frac{dl}{B_p x^2}. \tag{30}$$

In the evaluation of the particle flux Γ and the heat fluxes $\langle \mathbf{q}_i \cdot \nabla \Phi \rangle$ and $\langle \mathbf{q}_e \cdot \nabla \Phi \rangle$, it is the anomalous part that dominates. We take this to be of the form

$$\Gamma_A = -\frac{D_1}{n^2} |\nabla \Psi|^2 (2\pi q)^2 \frac{\partial n}{\partial \Phi}, \tag{31a}$$

$$\langle \mathbf{q}_e \cdot \nabla \Phi \rangle_A = -D_2 |\nabla \Psi|^2 (2\pi q)^2 \frac{\partial T_e}{\partial \Phi}, \tag{31b}$$

$$\langle \mathbf{q}_i \cdot \nabla \Phi \rangle_A = -D_3 |\nabla \Psi|^2 (2\pi q)^2 \frac{\partial T_i}{\partial \Phi}. \tag{31c}$$

We have taken $(D_1, D_2, D_3) = (0.1, 1.0, 1.0) \times 10^{19}\ \mathrm{m}^{-1}\mathrm{sec}^{-1}$ to give a reasonable fit to PBX data.

B. *Vacuum Region*

The vacuum region is defined by either having $\Psi > \Psi_L$, where Ψ_L is the first plasma flux surface in contact with a limiter or by being separated from the plasma by a magnetic x point. We treat the vacuum region as a low temperature, zero pressure gradient plasma in which currents can appear. In the limit as the vacuum conductivity approaches zero, the magnitude of these currents will go to zero and the magnitude of the magnetic diffusion coefficient will approach infinity. Thus, Eq. (6) (with $\nabla p = 0$), and Eqs. (9) and (10) are solved in the vacuum region, with a classical resistivity, Eq. (26), based on a constant electron temperature $T_e = T_v$. The vacuum temperature, normally a few eV, is much less than the central plasma temperature, normally 0.1 to 3.0 keV; however, it is not zero. This vacuum temperature and a vacuum density, n_v, serve as boundary conditions on the surface-averaged plasma evolution Eqs. (14) through (16). Since the plasma temperatures and densities will approach these values smoothly, all physical quantities are smooth and continuous across the plasma-vacuum interface, and no special boundary treatment is required there. Again, we must verify a posteriori that the physical results converge to a value independent of the vacuum temperature T_v.

At the outer boundary of the vacuum region, i.e., the computational domain boundary, we model an insulating, magnetically transparent boundary by prescribing that the toroidal field strength g and the poloidal flux Ψ be consistent with the instantaneous plasma and coil currents. Thus, on the boundary points $\mathbf{x}_b$,

$$g(\mathbf{x}_b) = g_0 = \frac{\mu_0 I_{TF}}{2\pi}, \tag{32}$$

$$\Psi(\mathbf{x}_b, t) = \frac{\mu_0}{2\pi} \int_p G(\mathbf{x}_b, \mathbf{x})\, J_\phi(\mathbf{x}, t)\, d^2\mathbf{x} + \sum_{i=1}^{N} \frac{\mu_0}{2\pi} G(\mathbf{x}_b, \mathbf{x}_i)\, I_i. \tag{33}$$

Here, I_{TF} is the total current in all the toroidal field coils, $G(\mathbf{x}_b, \mathbf{x})$ is the analytic exterior Green's function for an axisymmetric current filament [11],

$J_\phi = (\mu_0 x)^{-1} \Delta^* \Psi$, and the integration and summation in Eq. (33) are over the plasma volume and discrete coils, respectively.

The two-dimensional integral in Eq. (33) is expensive to evaluate numerically, having to be performed at each boundary point each time-step. We therefore analytically expand the Green's function $G(\mathbf{x}_b, \mathbf{x})$ about the current centroid source point

$$G(\mathbf{x}_b, \mathbf{x}) = G(\mathbf{x}_b, \mathbf{x}_0) + (\mathbf{x} - \mathbf{x}_0) \cdot \nabla G(\mathbf{x}_b, \mathbf{x})|_{\mathbf{x}_0} + \tfrac{1}{2} (\mathbf{x} - \mathbf{x}_0)(\mathbf{x} - \mathbf{x}_0) : \nabla\nabla G(\mathbf{x}_b, \mathbf{x})|_{x_0} + \cdots . \tag{34}$$

If we perform the expansion, Eq. (34), about the current centroid

$$\mathbf{x}_0(t) = \frac{1}{I(t)} \int_p \mathbf{x} J_\phi(\mathbf{x}, t)\, d^2\mathbf{x} \tag{35}$$

with

$$I(t) = \int_p J_\phi(\mathbf{x}, t)\, d^2\mathbf{x}, \tag{36}$$

then the integral appearing in Eq. (33) becomes

$$\int_p G(\mathbf{x}_b, \mathbf{x})\, J_\phi(\mathbf{x}, t) = G[\mathbf{x}_b, \mathbf{x}_0(t)]\, I(t) + \tfrac{1}{2} \mathbf{K}(t) : \nabla\nabla G(\mathbf{x}_b, \mathbf{x})|_{\mathbf{x}_{0(t)}} + \cdots \tag{37}$$

with the quadrupole tensor defined by

$$\mathbf{K} = \int_p [\mathbf{x} - \mathbf{x}_0(t)][\mathbf{x} - \mathbf{x}_0(t)]\, J_\phi(\mathbf{x}, t)\, d^2\mathbf{x}. \tag{38}$$

The normal component of the momentum density at the boundary consistent with Eqs. (32), (33), and (6)–(10) with the inertial terms vanishing is

$$x\hat{n} \cdot (\nabla\Omega + \nabla\phi \times \nabla A) = \frac{-\rho_0}{B^2 x} \frac{\partial \Psi}{\partial t} \hat{n} \cdot \nabla\Psi \equiv N(\mathbf{x}_b, t). \tag{39}$$

Thus, if $\hat{n}$ and $\hat{l} = \hat{n} \times \hat{\phi}$ are the directions normal and tangential to the boundary, we have the boundary conditions

$$\frac{\partial A}{\partial l} = N(\mathbf{x}_b, t) - \bar{N}(t), \tag{40}$$

$$x \frac{\partial \Omega}{\partial n} = \bar{N}(t), \tag{41}$$

where $\bar{N}(t)$ is the average value of $N(\mathbf{x}_b, t)$ on the boundary,

$$\bar{N}(t) \equiv \frac{\oint N(\mathbf{x}_b, t)\, dl}{\oint dl}. \tag{42}$$

The decomposition of the normal boundary velocity as prescribed by Eqs. (39)–(42) is not unique. Indeed, consider the transformation where we add to the velocity field two functions A_H and Ω_H such that

$$A \to A + A_H, \tag{43a}$$

$$\Omega \to \Omega + \Omega_H, \tag{43b}$$

with

$$\nabla^2 \Omega_H = \Delta^* A_H = 0 \tag{43c}$$

in the interior and

$$\frac{1}{x}\frac{\partial A_H}{\partial l} + \frac{\partial \Omega_H}{\partial n} = 0 \tag{43d}$$

on the boundary. Such a transformation leaves all physical quantities unchanged.

Finally, we note that the error one would introduce by using homogeneous boundary conditions; i.e., Eqs. (40) and (41) with $U = 0$, would not be large. An acceleration term would be forced to appear near the boundary obeying

$$\frac{\partial \mathbf{v}}{\partial t} = \nu \nabla^2 v - \frac{B^2}{\eta \rho_0}\left(\frac{1}{B^2 x^2}\frac{\partial \Psi}{\partial t}\nabla \Psi + \mathbf{v}\right). \tag{44}$$

This would result in an unphysical boundary layer velocity gradient of thickness $d = (\eta_v / B_0)(\rho_0/\mu_0)^{1/2}$ in which the velocity is accelerated to the value of Eq. (39).

C. *Solid Conductors*

The physical material velocity is zero in the solid conductors. Allowing for the possibility of an external circuit connection supplying an applied voltage $V(t)$, the poloidal flux evolution equation, the analogue of Eq. (9) in the plasma, becomes

$$\frac{\partial}{\partial t}\Psi = \mu_0^{-1} \eta \Delta^* \Psi + (2\pi)^{-1} V(t). \tag{45}$$

We note here a direct analogy between the poloidal flux evolution equation in the conductor, Eq. (45), and a discrete circuit equation. Suppose a single isolated mesh

point $(x, z) = (x_i, z_j)$ is treated as a solid conductor. The mesh point has associated an area $\Delta A = \Delta x \Delta z$, a resistance $r_{i,j}$, and a current $I_{i,j}$ given by

$$r_{i,j} = \frac{2\pi\eta_{i,j}x_i}{\Delta A}, \tag{46}$$

$$I_{i,j} = \frac{\Delta A \Delta^* \Psi_{i,j}}{\mu_0 x_i}. \tag{47}$$

The poloidal flux at the mesh point is due to a self-inductance and a mutual inductance part,

$$-2\pi\Psi_{i,j} = L_{i,j}I_{i,j} + \sum_{i'j'}{}' M_{i,j;i'j'}I_{i'j'}, \tag{48}$$

where the sum is over all other currents, being in the grid conductors, the plasma, and external to the grid. The mutual inductance in Eq. (48) is the Green's function appearing in Eq. (33),

$$M_{i,j;i',j'} = \mu_0 G(\mathbf{x}_{i,j}, \mathbf{x}_{i',j'}), \tag{49}$$

while $L_{i,j}$, the intrinsic inductance of a mesh point, is obtained by substitution of the asymptotic small argument expansion for G into the five-point-centered finite difference representation of Eq. (47). Thus, taking $\Delta x = \Delta z$, we have

$$L_{i,j} = \mu_0 x_i \left[\ln\left(\frac{8x_i}{\Delta x}\right) - \frac{\pi}{2} \right]. \tag{50}$$

With the definitions in Eqs. (46) through (50), we see that the discrete form of Eq. (45) becomes

$$\frac{d}{dt}\left(L_{i,j}I_{i,j} + \sum_{i'j'}{}' M_{i,j;i'j'}I_{i'j'} \right) + r_{i,j}I_{i,j} + V(t) = 0. \tag{51}$$

The differential form, Eq. (45), is actually used, but it is useful to keep this correspondence in mind.

To model the control systems in the tokamak, we allow the applied voltage $V(t)$ appearing in Eqs. (45) and (51) to be a function of the instantaneous poloidal flux values at two or more observation points $\mathbf{x}^{\mathrm{OBS}}$, and of other global parameters. A useful form for most applications is to specify the positions of two observation points $\mathbf{x}_1^{\mathrm{OBS}}$ and $\mathbf{x}_2^{\mathrm{OBS}}$, a linear gain α and a normalized flux offset β so that

$$V(t) = \alpha \left[\Psi(\mathbf{x}_1^{\mathrm{OBS}}) - \Psi(\mathbf{x}_2^{\mathrm{OBS}}) - \frac{\beta I_p(t)}{I_{p0}} \right], \tag{52}$$

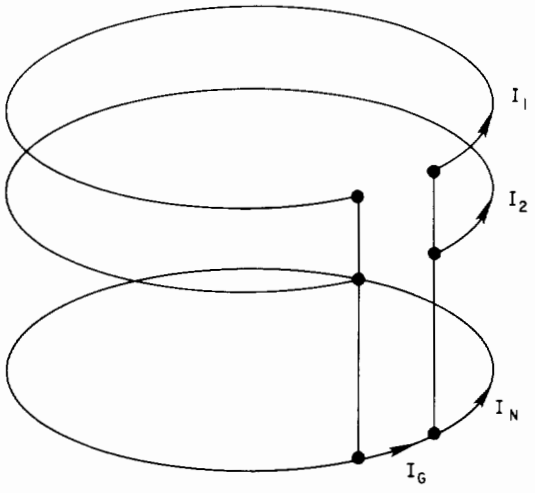

FIG. 2. Generalized poloidal field circuit configuration allows for a gap with gap current I_G and gap resistivity r_G.

where $I_p(t)$ and I_{p0} are instantaneous and reference values of the total plasma current.

It is necessary to generalize the circuit Eq. (45) to model conductors with toroidal cuts or toroidally localized high resistance regions such as bellows or vacuum vessels with toroidal breaks. We take a group of N poloidal field conductors to be connected as in Fig. 2 with a small common gap with gap resistance r_G and gap current

$$I_G = \sum_{n=1}^{N} I_n = \Delta A \sum_{n=1}^{N} \mu_0^{-1} \Delta^* \Psi_n / x_n. \tag{53}$$

The generalization to Eq. (45) is then simply, for $n = 1, N$,

$$\frac{\partial}{\partial t} \Psi_n = \mu_0^{-1} \eta_n \Delta^* \Psi_n + (2\pi)^{-1} [V_n(t) + r_G I_G]. \tag{54}$$

We verify that Eqs. (53) and (54) have the correct limits, reducing to Eq. (45) when $r_G \to 0$ and forcing $I_G = 0$ when $r_G \to \infty$.

Finally, we consider the boundary conditions on the velocity variables A and Ω at the interface between the conductors and the vacuum region. For the same considerations as discussed in Section IIB the appropriate boundary conditions are given by Eq. (39). However, imposing internal boundary conditions and thus making the computational region multiply connected would rule out the use of fast

elliptic solvers to invert the elliptic operators for Ω and for A. Instead, we define $\nabla^2\Omega$ and Δ^*A inside the conductor region as

$$\nabla^2\Omega = \nabla\cdot\left(-\frac{\rho_0}{B^2x^2}\frac{\partial\Psi}{\partial t}\nabla\Psi\right), \tag{55}$$

$$\Delta^*A = x^2\nabla\cdot\left(-\frac{\rho_0}{B^2x^2}\frac{\partial\Psi}{\partial t}\nabla\Psi\times\nabla\phi\right). \tag{56}$$

Outside the conductors, this appears equivalent to defining boundary values for A and $\partial\Omega/\partial n$ from Eq. (39).

III. Numerical Methods

A. *Two-Dimensional Variables*

The variables are defined at staggered locations on an equally spaced Cartesian grid. This leads to a scheme consistent with the imposition of accurate boundary conditions, and one that couples together the minimum number of grid points. As shown in Fig. 3, the variables Ψ, A, and Δ^*A are defined to lie on grid line intersections, while the variables g, ω, Ω, and $\nabla^2\Omega$ lie on cell centers.

As discussed previously, by artificially enhancing the plasma density, the frequencies of the Alfvén wave oscillations are greatly reduced. However, there remain disparate time scales in the equations due to the differences in the propagation speeds

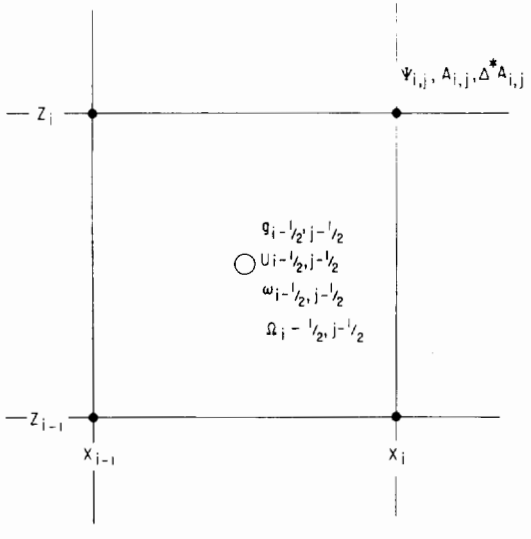

FIG. 3. The variables Ψ, A, Δ^*A are defined at grid point intersection (integers) while g, U, ω, ∇^2U are defined at cell centers (half integers). Note that $\Psi_{i,j}\equiv\Psi(x_i, z_j)$, etc.

of the compressible and transverse Alfvén waves, and also due to the differences between the value of the resistivity in the hot plasma and in the cold vacuum regions. We therefore use the technique of subcycling to evaluate the diffusive and fast wave terms N times (typically $N = 10$–80) during each time-step used by the rest of the problem. This leads to a considerable time savings since the subcycled terms are relatively simple and are evaluated in a tight loop well-suited to a vector computer.

We introduce a variable U for the divergence of the velocity, $U = \nabla^2 \Omega$. The forms of Eqs. (6a), (9), and (10) appropriate to apply subcycling are

$$\frac{\partial U}{\partial t} + \mu_0^{-1} g_0 \nabla \cdot \frac{1}{x^2} \nabla g + Q = \nabla \cdot \nu_2 \nabla U, \tag{57}$$

$$\frac{\partial}{\partial t} \Psi + S = \mu_0^{-1} \eta_\parallel \Delta^* \Psi, \tag{58}$$

$$\frac{\partial}{\partial t} g + \rho_0^{-1} g_0 U + T = \mu_0^{-1} x^2 \nabla \cdot \frac{\eta_\parallel}{x^2} \nabla g, \tag{59}$$

where g_0/x, as in Eq. (32), is the toroidal field strength away from the plasma, and the slowly varying Q, S, and T are defined as

$$Q = \nabla \cdot \left(\frac{\Delta^* \Psi}{\mu_0 x^2} \nabla \Psi + \frac{g - g_0}{\mu_0 x^2} \nabla g + \nabla p \right), \tag{60}$$

$$S = \rho_0^{-1} (\nabla \phi \times \nabla A \cdot \nabla \Psi + \nabla \Omega \cdot \nabla \Psi), \tag{61}$$

$$T = x^2 \nabla \cdot \left(\frac{g}{\rho_0 x^2} \nabla \phi \times \nabla A + \frac{g - g_0}{\rho_0 x^2} \nabla \Omega - \frac{\omega}{\rho_0 x^2} \nabla \phi \times \nabla \Psi \right) + g_0 x^2 \nabla \Omega \cdot \nabla \frac{1}{\rho_0 x^2}. \tag{62}$$

Thus, Eqs. (57)–(59) for U, Ψ, and g are updated N times with a time-step $\delta t = \Delta t / N$ for each major time-step when Q, S, and T are evaluated from Eqs. (60)–(62), $\Delta^* A$ and ω are updated from Eqs. (6b) and (6c), the surface-averaged equations for N', σ, σ_e are advanced, and the elliptic equations for A and Ω are inverted. An explicit time advancement scheme is utilized, in which the wave and convection terms are differenced by using the leapfrog method [12] and the diffusive terms by using a mix of a forward-time centered-space method and the method of Dufort and Frankel [12]. Thus, for example, Eq. (59) is differenced as

$$\begin{aligned} &\frac{1}{2\delta t} (g_{i,j}^{n+1} - g_{i,j}^{n-1}) + \rho_0^{-1} g_0 U^n + T \\ &\quad = \frac{1}{\mu_0 (\Delta x)^2} \left[\eta_{i+1/2;j} \left(\frac{x_i}{x_{i+1/2}} \right) \{ \theta [g_{i+1,j}^n - \tfrac{1}{2} (g_{i,j}^{n+1} + g_{i,j}^{n-1})] \right. \end{aligned}$$

$$
\begin{aligned}
&+(1-\theta)(g_{i+1,j}^{n-1}-g_{i,j}^{n-1})\}\\
&-\eta_{i-1/2,j}\left(\frac{x_i}{x_{i-1/2}}\right)\{\theta[\tfrac{1}{2}(g_{i,j}^{n+1}+g_{i,j}^{n-1})-g_{i-1,j}^{n}]\\
&+(1-\theta)(g_{i,j}^{n-1}-g_{i-1,j}^{n-1})\}\Big]\\
&+\frac{1}{\mu_0(\Delta z)^2}\,[\eta_{i,j+1/2}\{\theta[g_{i,j+1}^{n}-\tfrac{1}{2}(g_{i,j}^{n+1}+g_{i,j}^{n-1})]\\
&+(1-\theta)(g_{i,j+1}^{n-1}-g_{i,j}^{n-1})\}\\
&-\eta_{i,j-1/2}\{\theta[\tfrac{1}{2}(g_{i,j}^{n+1}+g_{i,j}^{n-1})-g_{i,j-1}^{n}]\\
&+(1-\theta)(g_{i,j}^{n-1}-g_{i,j-1}^{n-1})\}].
\end{aligned}
\tag{63}
$$

Here, $0<\theta<1$ measures the relative mix between the two difference schemes, superscript n denotes time (sub) cycle, and subscript i and j denote x and z locations. Equation (63) is solved algebraically for $g_{i,j}^{n+1}$ at each location, with T being recomputed only every N subcycles.

The condition for stability of the wave terms is that, assuming $\Delta x=\Delta z$,

$$
\delta t \lesssim \frac{\Delta x(\mu_0\rho_0)^{1/2}}{(8)^{1/2}\,B_{\mathrm{T}}} \tag{64}
$$

and

$$
\Delta t = N\delta t \lesssim \frac{\Delta x(\mu_0\rho_0)^{1/2}}{(2)^{1/2}\,B_{\mathrm{p}}}, \tag{65}
$$

where B_{p} and B_{T} denote the poloidal and toroidal field strengths. If we set $N=2B_{\mathrm{T}}/B_{\mathrm{p}}$, then the two criteria become identical. The explicit differencing of the diffusive terms imposes a time-step restriction for stability,

$$
\delta t < \frac{\mu_0(\Delta x)^2}{8\eta_{ij}(1-\theta)}. \tag{66}
$$

The restriction in Eq. (66) appears to be avoidable by letting $\theta\to 1$. However, we find empirically that for $\theta\gtrsim 0.9$, the odd and even space and time points can become decoupled, leading to numerical instability.

B. *Surface-Averaged Variables*

The one-dimensional surface-averaged Eqs. (14), (15), (16), and (24) for N', σ, σ_{e}, and ι are integrated in time simultaneously with the two-dimensional equations using the numerical scheme described in Section 3 of Ref. [13]. The transport quan-

tities Γ, Q_e, Q_i, and V_L are allowed to be linear combinations of any functions multiplying gradients of n, p, p_e, or q^{-1}. We note here that N', σ, σ_e, and ι are the adiabatic variables, so that if $\Gamma = Q_e = Q_i = V_L = 0$ and if all the sources vanish so that $S_N = S_e = S_i = 0$ and $Q_{\Delta e} = 0$, these quantities are exactly conserved. The finite difference method used here will preserve this property.

Every few time-steps, the surface-averaged quantities $dV/d\Phi$, K, and α are evaluated by performing contour integrals on $\Psi = \text{constant}$ surfaces using the definitions in Eqs. (17), (19), and (30). The contour integrals are evaluated at N_c points, equally spaced in toroidal flux, $\Delta\Phi = 2\pi q \Delta\Psi$. The number of points N_c may change during the time evolution so that the range of toroidal flux can accommodate a growing or shrinking plasma region $0 < \Phi < \Phi_p$ with the increments $\Delta\Phi$ remaining fixed.

The surface-averaged transport densities N', σ, σ_e, ι are defined at cell centers, or half-integer values, to allow accurate treatment of the boundary and the magnetic axis, e.g., $\iota_{j-1/2} \equiv \iota(\Phi_{j-1/2})$. A matrix Crank–Nicolson [12, 13] implicit scheme is used to advance variables from time-step n to $n+1$. Thus, for example, Eqs. (24) and (29) for the transform become

$$A_j \iota_{j+1}^{n+1} - B_j \iota_j^{n+1} + C_j \iota_{j-1}^{n+1} + D_j = 0, \tag{67}$$

with

$$A_j = s a_{j+1/2} b_{j+1}, \tag{68a}$$

$$C_j = s a_{j-1/2} b_{j-1}, \tag{68b}$$

$$B_j = 1 + s(a_{j+1/2} + a_{j-1/2})\, b_j, \tag{68c}$$

$$D_j = \iota^n + \Delta t(1-\theta)\frac{\partial}{\partial \Phi} V_L^n. \tag{68d}$$

Here, $s = \Delta t\theta/(\Delta\Phi)^2$, $a_j = (2\pi)^2\ \eta_{\parallel j}/(\alpha_j^2 \iota_j^2)$, $b_j = K_j \alpha_j$, and $0 < \theta < 1$ is again a parameter measuring the implicitness of the method.

After many time steps the transform $\iota(\Phi)$ obtained from integrating Eq. (24), i.e., evaluating Eq. (67), will not exactly agree with that obtained from integrating Eqs. (9) and (10). The difference is due to the differences in the finite-grid truncation error. To avoid accumulating error, we correct the two-dimensional toroidal field function $g(x, z)$ from its value as computed from Eq. (63). Thus, if $g_{i,j}^{n+1}$ is the value as computed from Eq. (63), we correct it as follows

$$\tilde{g}_{i,j}^{n+1} = g_{i,j}^{n+1} + \frac{\Delta t}{\tau}\left(\frac{2\pi}{\alpha_{i,j}\iota_{i,j}^{n+1}} - g_{i,j}^{n+1}\right). \tag{69}$$

Here, τ is a relaxation time, typically $\tau = 10\,\Delta t$.

IV. Code Verification

A. *Green's Function Expansion Test*

To test the accuracy of the Green's function expansion method for updating the boundary poloidal magnetic flux, Eqs. (33) and (37), we have computed the exact value of the poloidal magnetic flux at the computational boundary for an elliptical cross-sectional equilibrium

$$\Psi_e(\mathbf{x}_b) = \frac{\mu_0}{2\pi} \int_p G(\mathbf{x}_b, \mathbf{x})\, J_\phi(x), \tag{70}$$

and also the values obtained by retaining only the first one and the first two terms in the expansion

$$\Psi_1(\mathbf{x}_b) = \frac{\mu_0}{2\pi} G(\mathbf{x}_b, \mathbf{x}_0)\, I(t), \tag{71}$$

$$\Psi_2(\mathbf{x}_b) = \Psi_1(\mathbf{x}_b) + \frac{1}{2}\frac{\mu_0}{2\pi} \mathbf{K}: \nabla\nabla G(\mathbf{x}_b, \mathbf{x})|_{\mathbf{x}_0}, \tag{72}$$

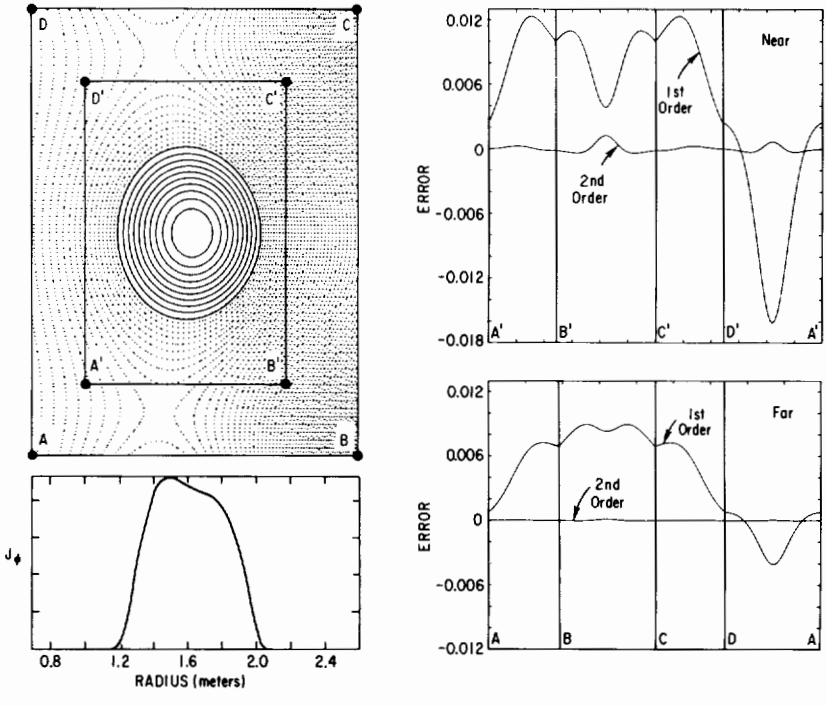

FIG. 4. Relative boundary error in keeping first and second correction terms in Green's expansion for two computational boundary locations.

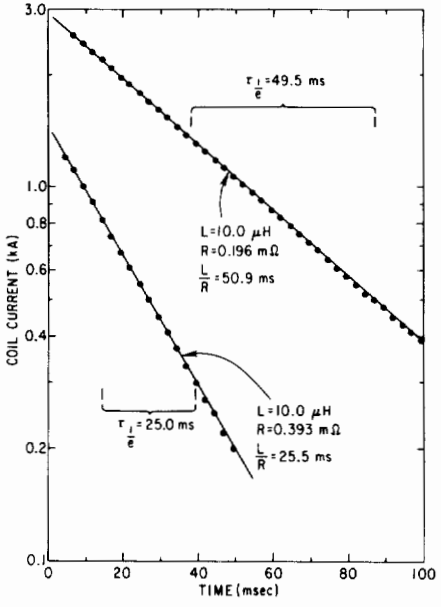

FIG. 5. Test conducted with coils present but without plasma exhibits exponential decay on L/R time of coils.

where $I(t)$, $\mathbf{x}_0$, and $\mathbf{K}$ are defined in Eqs. (35), (36), and (38). We display graphically in Fig. 4 the relative errors in the boundary flux due to truncating the expansion after the first and second terms, i.e., we plot normalized values of $[\Psi_1(\mathbf{x}_b) - \Psi_e(\mathbf{x}_b)]$ and $[\Psi_2(\mathbf{x}_b) - \Psi_e(\mathbf{x}_b)]$ for computational boundaries separated from the plasma by about 0.5 and 1.0 minor radii. The expansion in Eq. (37) is seen to be rapidly converging, yielding 10^{-3} relative errors when keeping only the first two terms for a boundary as close as 0.5 minor radii.

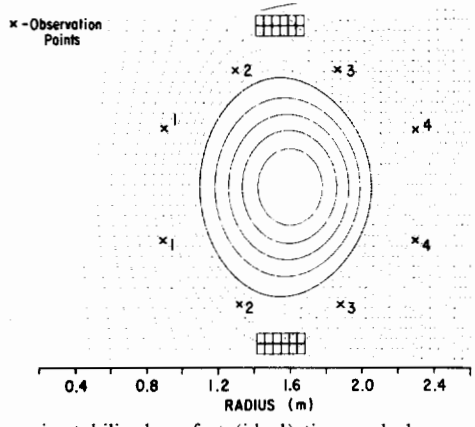

FIG. 6. Elliptical plasma is stabilized on fast (ideal) time scale by conducting plates. Observation points record flux difference of instability caused by finite resistivity of conductors.

B. *Coils Only Decay Test*

To verify that the circuits part of the code is computed correctly, we set up a test problem with two coils located symmetrically above and below the midplane at ($x = 1.2$, $z = \pm 0.75$). The remainder of the computational region, $0.38 < x < 2.6$, $-1.6 < z < 1.6$ is a vacuum, i.e., 1.5 eV resistive plasma with zero pressure gradient. The number of spatial grid points in x and z were 49 and 57, respectively. At $t = 0$, the coils are initialized with equal and opposite currents. As time advances, the coil currents decay and we plot their currents versus time for two cases with different coil resistivity in Fig. 5 comparing with the exact L/R decay time. The agreement is seen to be excellent.

C. *Resistive Axisymmetric Stability Test*

A model problem consisting of an elliptical cross-sectional plasma and top–bottom finite resistivity plates is set up as shown in Fig. 6. At $t = 0$, the plasma is given a perturbation by applying a radial magnetic field to induce asymmetry in the vertical direction. The conducting plates stabilize the plasma on the ideal MHD, Alfvén wave transit time scale, but an instability persists on the much slower time

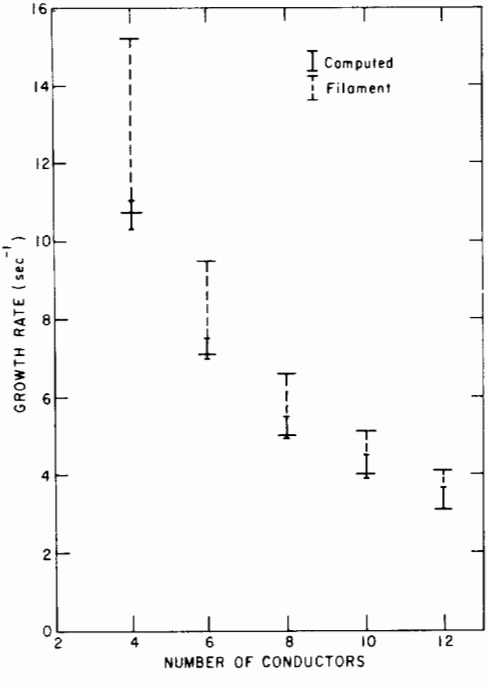

FIG. 7. Growth rates versus conductor size for elliptical plasma instability of Fig. 6. Also shown are predictions of a wire filament model located within $\pm 4\%$ of the minor radius about the current centroid.

scale characteristic of the resistive L/R time of the conducting plates. Pairs of observation points, symmetrically located above and below the plasma midplane record the value of the poloidal magnetic flux versus time. The difference in the flux measurements between the members of a pair give a measure of the plasma displacement. The flux differences exhibit exponential growth and from these we calculate a growth rate.

We plot in Fig. 7 the range of growth rates obtained from these flux measurements for different size conducting plates, and for comparison, the growth rates obtained assuming the plasma was a filamentary conductor located on the midplane within $\pm 4\%$ of the minor radius about the current centroid.

D. *Scaling Tests*

We have taken one of the cases of Fig. 7, with 12 conductors, and have rerun it repeatedly, changing a single numerical parameter each time, and record how the measured growth rate varies. We seek to verify the theoretical predictions that the growth rate is proportional to the resistivity in the plates and is independent of the plasma mass, vacuum resistivity, and other numerical parameters.

The results of these scaling tests are illustrated in Fig. 8. Where we plot a single growth rate, it represents an average over the four observation pairs for each case. We see that to within the error bars on our growth rate measurements, the results are independent of factor of two variations in the plasma mass, location of computational boundary, computational zone size, numerical viscosity, plasma

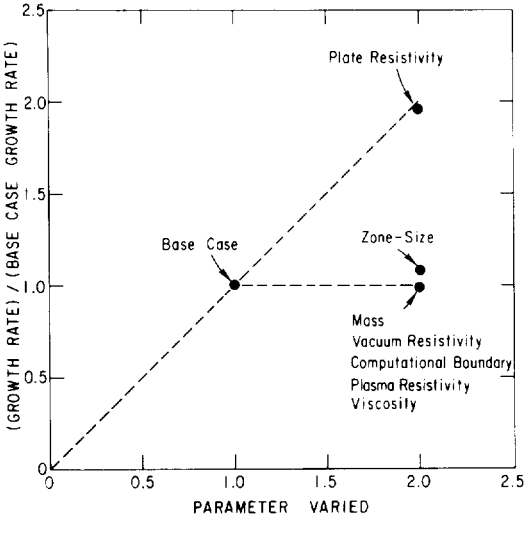

FIG. 8. Scaling tests on 12 conductor case of Fig. 7. Growth rate is computed with (1) plate resistivity doubled, (2) plasma mass doubled, (3) computational boundary distance doubled, (4) zone size doubled, (5) viscosity doubled, (6) vacuum resistivity doubled, and (7) plasma resistivity doubled.

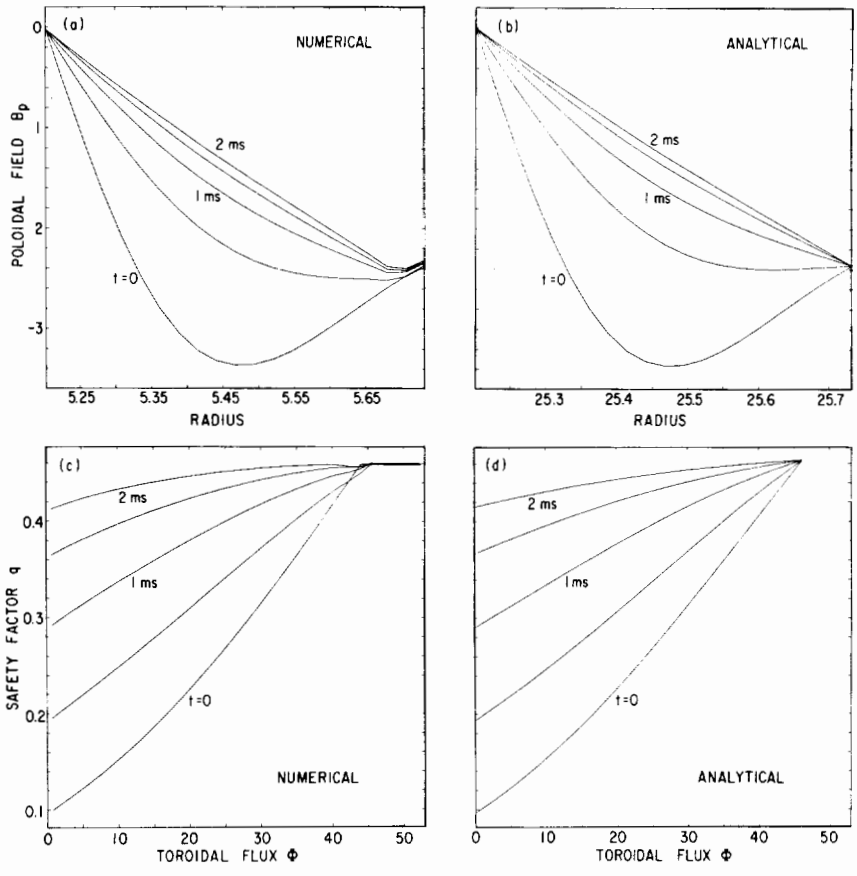

FIG. 9. Comparison of computed and analytical solutions for large aspect ratio field diffusion test with constant resistivity.

resistivity, and vacuum resistivity. In addition, the growth rate scales linearly with a factor of two increase in the conductor resistivity.

E. *Field Diffusion Test*

We have set up a test problem to compute poloidal magnetic field diffusion in a large aspect ratio, circular cross-sectional plasma with uniform plasma resistivity so that an approximate analytical solution is valid. A numerical equilibrium is formed with $x_0 = 25.2$ m, $a = 0.5$ m, and with an initially peaked current distribution. We let the system evolve with the ohmic heating system on to keep the total plasma current constant in time, $I_p = 6$ MA. In Figs. 9a and 9c we plot the computed profiles of the poloidal magnetic field, $B_p = |\nabla\Psi|/x$ as computed from Eqs. (9) and (27), and the safety factor $q \equiv (2\pi)^{-1}\, d\Phi/d\Psi$ as computed from Eqs. (24) and (29)

TABLE I

PBX Coil System

	R	Z	Turns
EF	1.650	±0.800	−7
	2.255	±0.600	−13
	2.255	±0.254	−8
SF	0.990	±0.065	−8
	1.932	±0.705	−3
	0.667	±0.600	+3
	0.667	±0.705	+3
	0.665	±0.071	+5
RF	1.210	±0.75	±8

at 0.5 msec intervals. For comparitive purposes, we also plot the approximate analytical solution in Figs. 9b and d,

$$B_\theta(r, t) = \frac{\mu_0}{2\pi}\frac{r}{a^2} I_p + \sum_{m=1}^{\infty} A_m J_1\left(\lambda_m \frac{r}{a}\right) \exp(-\lambda_m^2 t/t_0), \tag{73}$$

where the coefficients A_m are obtained from initial conditions

$$A_m = \frac{2}{[J_0(\lambda_m)]^2}\left\{\frac{1}{a^2}\int_0^a dr\, rB_\theta(r, 0)\, J_1\left(\lambda_m \frac{r}{a}\right) - B_\theta(a, 0)\frac{J_2(\lambda_m)}{\lambda_m}\right\}. \tag{74}$$

Here, $t_0 = \mu_0 a^2/\eta = 8.16$ ms is the skin time, $r \equiv [(x-x_0)^2 + z^2]^{1/2}$, the J_i are Bessel functions, and the λ_m are zeros of J_1. The safety factor q for the analytical solutions is calculated from $q = rB_T^0/RB_p(r, t)$, with the toroidal flux $\Phi = \pi r^2 B_T^0$, and the toroidal field B_T^0 taken as constant.

TABLE II

PBX Preprogrammed Trajectories

Time (sec)	0.0	0.025	0.135	0.175	0.275
$I_p(kA)$	100	200	325	375	525
$I_{EF}(kA)$	1.19	2.0	3.60	6.0	12.0
$I_{SF}(kA)$	0.0	0.0	4.0	7.0	14.0
$P_0(N-m^2)$	2400	4800	7600	10,000	60,000

V. Application to PBX

As an illustration of the application and use of this method, we present a simulation of the current buildup and shaping phase of the plasma in the PBX experiment at the Princeton Plasma Physics Laboratory. Detailed comparison of the predictions of this code with the actual magnetic measurements from the experiment will be presented in a companion publication.

The PBX coil systems are summarized in Table I. The equilibrium field (EF) system provides a relatively uniform vertical field, while the shaping field (SF) system is such as to indent the plasma and deform it into a kidney bean shape. A radial field (RF) system is connected to a feedback amplifier so as to keep the plasma centered on the midplane. Three passive conducting plate systems are

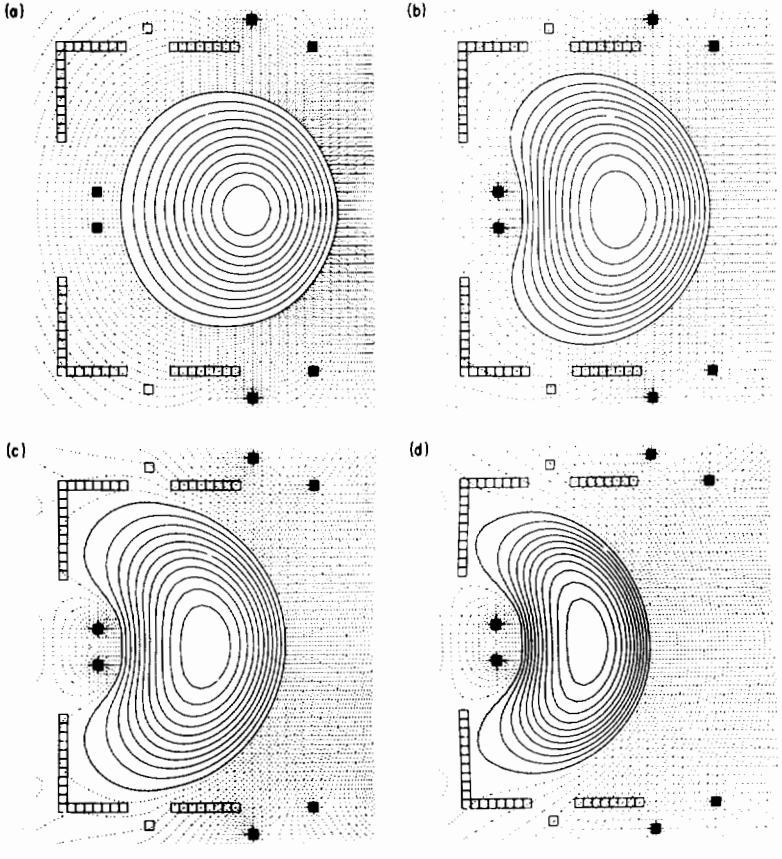

FIG. 10. Snapshots of computed poloidal flux surfaces in PBX experiment at times $t = 0.0$, 150, 200, 300 ms during current ramp-up and shaping phase.

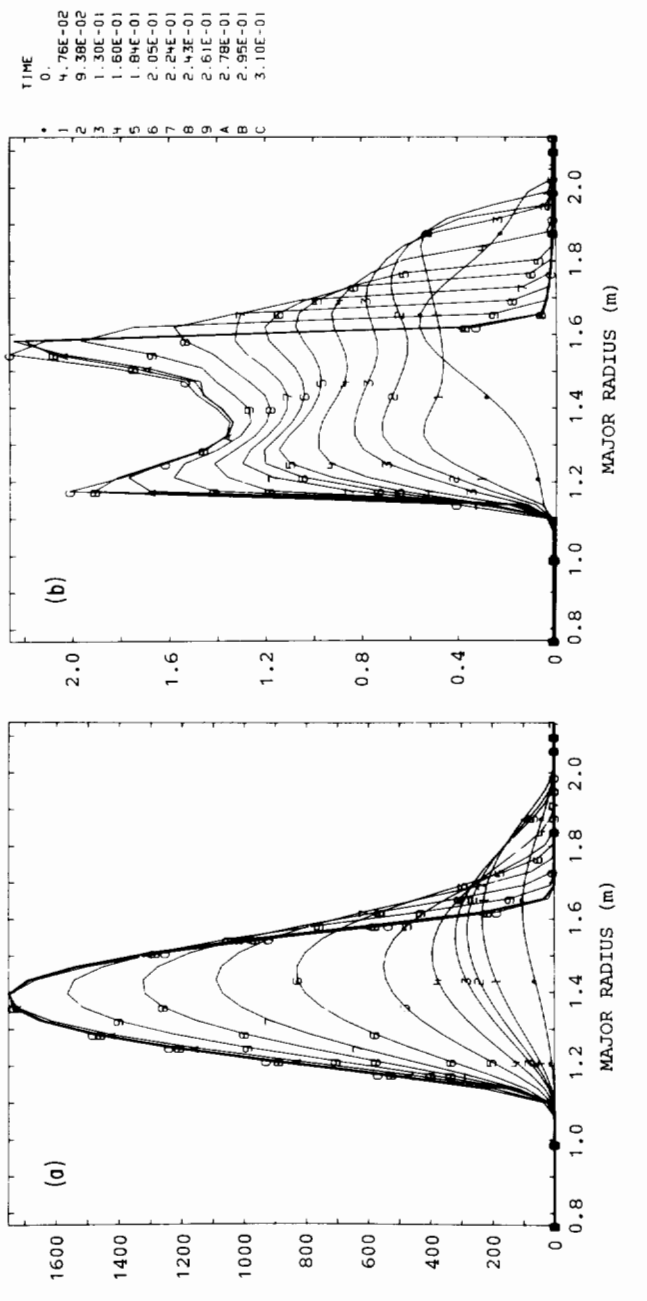

FIG. 11. Profiles across midplane of (a) plasma pressure and (b) toroidal current density for PBX calculation of Fig. 10.

installed to stabilize the plasma axisymmetric modes on the fast ideal MHD time scale. These are connected in top–bottom pairs so that no net current can flow through an antisymmetric pair.

The ohmic heating (OH) system is modeled by a "perfect" OH system, which increases the value of the poloidal flux uniformly on the plasma boundary at a rate that keeps the total plasma current on the trajectory described in Table II. The other coil systems also have voltages applied, as described in Eq. (45), to keep the currents on specified trajectories. For the EF and RF systems, these nominal

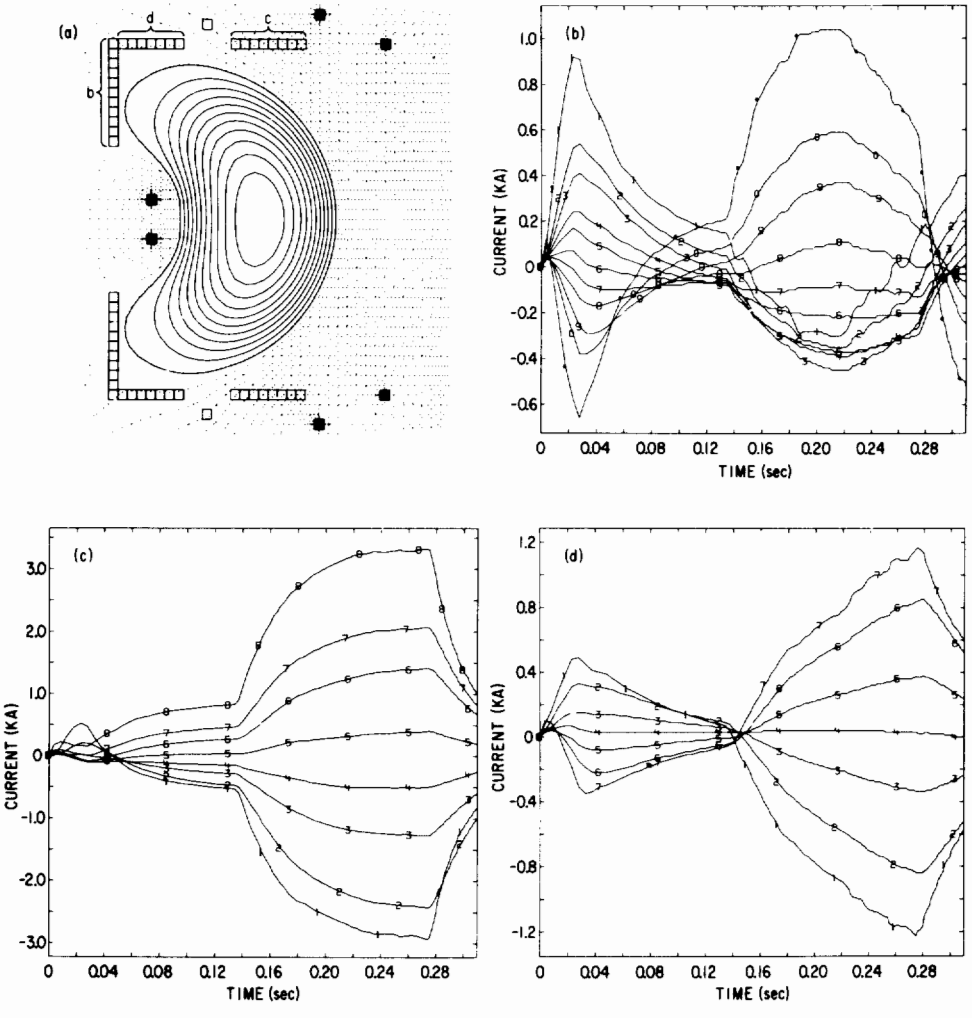

FIG. 12. Time history of current distribution in passive conducting plate segments for PBX calculation of Fig. 10.

current trajectories are modified by feedback signals to provide radial and vertical position control. Thus,

$$I_{EF}(t) = I^0_{EF}(t) + \alpha_1[\Psi(1.1, 0.0, t) - \Psi(2.0, 0.0, t) + \delta], \tag{75a}$$

$$I_{RF}(t) = \alpha_2[\Psi(1.01, 0.12, t) - \Psi(1.01, -0.12, t)], \tag{75b}$$

where $\delta = -0.025 \times [I_p(t)/I_p(\infty)] \times [I_{SF}(t)/I_{SF}(\infty)]$ is an offset, $I^0_{EF}(t)$ is the trajectory described in Table II, $\alpha_1 = 4 \times 10^3$ and $\alpha_2 = 2 \times 10^7$ are proportionality constants, and $\Psi(x, z, t)$ is the value of the poloidal magnetic flux per radian at location x, z at time t.

We illustrate in Fig. 10 the poloidal magnetic flux surfaces at several times during the simulation. The profiles of the toroidal current and pressure across the plasma midplane are shown in Fig. 11. It is seen that the current peaks on the outside of the discharge during the current ramp-up phase but eventually penetrates into the plasma. In Fig. 12 we plot the distribution of induced axisymmetric eddy currents in the three sections of passive conducting plates in the upper half of PBX. The presence of a gap in each of the plates constrains the net current in each of the plates to be zero.

One measure of the accuracy of the simulation is the ratio of the kinetic energy to the magnetic energy in the computational domain. This quantity remained smaller than 5×10^{-6} during the entire calculation, verifying that the inertial terms in the force balance Eq. (6) are indeed always small. This implies that the plasma evolves through a series of near-equilibrium states.

VI. Summary

We have described a new method for computing the free boundary time evolution of an axisymmetric toroidal plasma evolving due to plasma transport and resistive dissipation, external heating, and changing currents in the poloidal field coils. The method is based on introducing several artificial parameters into the zero inertia MHD and vacuum equations, and by taking the limit as these parameters become small. Code verification examples were presented as well as an application demonstrating the formation and positional stability of a bean-shaped plasma in the PBX device.

The present method does not solve the adiabatic equilibrium (Grad–Shafranov–Schlüter) equation each time-step, but rather evolves a velocity field through a modified equation of motion, Eq. (6), which forces the system to remain very close to equilibrium. Instead of solving elliptic equations for the poloidal flux in the vacuum region, we take the vacuum as the limit of a very high resistivity, zero pressure gradient plasma and solve a parabolic equation, Eqs. (9) and (27) for the evolution of the poloidal flux. In the plasma region itself, the adiabatic variables describing the differential number density, the differential total and electron entropy

density, and the rotational transform are also advanced by Eqs. (14), (15), (16), and (24).

The method is especially well suited to modeling problems in which the plasma is interacting with nearby conductors. Since the equation for the poloidal flux evolution does not change its type across plasma-vacuum or vacuum-conductor interfaces, matching problems are eliminated and the solution procedure simplifies greatly. Since the equilibrium equation is solved only to initialize at time $t = 0$, there are no bifurcation or nonconvergence difficulties.

ACKNOWLEDGMENTS

This work was performed in close collaboration with the PBX group at PPPL; M. Okabayashi and H. Takahashi, in particular. We were encouraged by F. W. Perkins and P. H. Rutherford and benefited by discussions with G. Bateman, M. Chu, R. C. Grimm, B. Merrill, J. Miller, and M. Reuch. Part of this work was completed while one of the authors (S.J.) was a guest at the Centre de Recherches en Physique des Plasmas at École Polytechnique Fédérale, Lausanne, Switzerland.

This work was supported by the U.S. D.O.E. Contract DE-ACO2-76-CHO-3073.

REFERENCES

1. F. TROYON *et al.*, *Eleventh European Conference on Controlled Fusion and Plasma Physics, Aachen, F.R.G.* 1983 (Ecole Polytechnique Fédérale de Lausanne, 1984, LRP 239/84.
2. M. OKABAYASHI, *et al.*, IAEA-CN-44/A-IV-3, 1984.
3. M. S CHANCE, J. C. JARDIN, AND T. STIX, *Phys. Rev. Lett.* **51**, 1963 (1983).
4. J. MANICKAM, R. C. GRIMM, AND M. OKABAYASHI, *Phys. Rev. Lett.* **51**, 1959 (1983).
5. R. C. GRIMM, *et al.*, Princeton Plasma Physics Laboratory Report No. PPPL-2090, 1984 (unpublished).
6. S. C. JARDIN, *Phys. Fluids* **21**, 10 (1978).
7. S. C. JARDIN AND D. LARRABEE, *Nucl. Fusion* **22**, 8 (1982).
8. K. BOL, *et al.*, "The Princeton Beta Experiment, PBX," Princeton Plasma Physics Laboratory Report No. PPPL–2032, 1983 (unpublished).
9. S. C. JARDIN AND W. PARK, Phys. Fluids **24**, 679 (1981).
10. S. P. HIRSHMAN AND S. C. JARDIN, *Phys. Fluids* **22** 731 (1979).
11. J. D. JACKSON, *Classical Electrodynamics* (Wiley, New York, 1975) 2nd ed., p. 177.
12. R. D. RICHTMYER AND K. W. MORTON, *Difference Methods for Initial Value Problems* (Interscience, New York, 1967).
13. S. C. JARDIN, *J. Comput. Phys.* **43**, 31 (1981).